Hindawi
International Journal of Energy Research
Volume 2023, Article ID 9727367, 17 pages
https://doi.org/10.1155/2023/9727367

Research Article

High-Fidelity Monte Carlo Analysis of Highly-Localized Fission Power Peaking near a Flux Trap in an MTR Core

Hadi Abuzlf,[1] **Christian Castagna**,[1] **Tzach Makmal**,[2] **Ofer Aviv**,[2] **Zohar Yungrais**,[2] **Guy Gabrieli**,[2] **Uri Steinitz**,[2] **Izhar Neder**,[2] **and Erez Gilad**[1]

[1]*The Unit of Nuclear Engineering, Ben-Gurion University of the Negev, Beer-Sheva 8410501, Israel*
[2]*Soreq Nuclear Research Centre, Yavne 8180000, Israel*

Correspondence should be addressed to Erez Gilad; gilade@bgu.ac.il

Received 23 May 2023; Revised 26 July 2023; Accepted 8 August 2023; Published 6 September 2023

Academic Editor: Sathish K. Kamaraj

In this study, a high-fidelity Monte Carlo model was utilized to investigate the localized behavior of the power peaking factor in a reactor core. The model considered the effect of water gaps, also known as flux traps, on the local power peaking. The model, developed using the Serpent code, employs a fine spatial mesh to accurately describe the fission power and burnup distribution. The results obtained from the model were validated through comparison with experimental measurements of the power distribution obtained from the IRR1 facility. The study found that the local accumulation of thermal flux caused by enhanced neutron moderation in the flux trap leads to a highly localized increase in power density, affecting the power peaking factor. The quantification of this effect was a key finding of the study. The results obtained from the study were highly dependent on the model's fidelity, with significant differences being observed between the power peaking factor calculated on a fine mesh as opposed to that calculated at the plate or assembly scale. Furthermore, the experimental validation of the model enabled the prediction of the power peaking factor in other regions within the fuel assembly, which are not accessible to measurement instrumentation, with a high degree of confidence. The study's findings may be useful for optimizing reactor design and operation and assessing the safety margins in reactors with similar characteristics.

1. Introduction

1.1. Computational Methods of Reactor Physics. The accurate evaluation of the fission power spatial distribution in the reactor core is a crucial aspect of nuclear reactors' design, operation, and safety. Various methods are employed to calculate reactor physics parameters, such as the power and flux distribution, energy spectrum, and fuel burnup. These methods include Monte Carlo and deterministic methods. These approaches provide complementary techniques for analyzing neutron behavior in a reactor and estimating key physical parameters.

Both Monte Carlo and deterministic methods have their strengths and limitations. Monte Carlo methods are accurate but computationally intensive, while deterministic methods are faster but involve approximations. In practice, a combination of these methods is often employed. Deterministic methods are used for preliminary calculations and reactor design optimization, while Monte Carlo simulations are utilized for detailed analysis, validation, and uncertainty quantification.

1.2. Deterministic Multigroup Diffusion Methods. Standard calculation techniques in large light-water power reactors adopt nodal diffusion methods that provide conservative solutions in a relatively short time [1–3]. Nodal diffusion methods have been used since the 1980s, and vast experience, knowledge, and know-how were accumulated and documented over the years [4, 5].

Nodal methods, by nature, calculate node-average or surface-average quantities, e.g., neutron flux, neutron current, and reaction rates. Therefore, nodal methods are inherently limited in evaluating the highly localized behavior of the neutron flux and possess fundamental uncertainties in studying localized subnodal effects [6–8]. One such effect is the impact of water gaps in the core on the surrounding local

thermal flux distribution and associated burnup distribution and power peaking factor (PPF).

Moreover, innovative reactor designs [9–12] are characterized by highly heterogeneous cores, giving rise to strongly localized flux gradients and spectral changes. To properly study these local effects, a high-resolution evaluation of the neutron flux distribution and the nuclei densities in the fuel is required compared to nodal diffusion methods.

1.3. The "Best Estimate" Approach. In recent years, there has been a growing interest in a promising alternative, the so-called "best estimate" methodology, based on high-fidelity Monte Carlo codes, e.g., Serpent [13], MCNP [14], and OpenMC [15], for detailed neutronic analyses characterized by high accuracy and flexible implementation [16–20]. This class of models, characterized by very fine spatial resolution, continuous energy spectrum, and continuous angular distribution, are referred to as high-fidelity models and allow detailed investigations of localized phenomena.

In this approach, advanced burnup analysis is possible [19], as well as coupling thermal-hydraulics and thermomechanical processes in the core (this coupling is not exclusive to Monte Carlo codes and can be done with deterministic codes). These new modeling approach strategies are often tested on research reactors and critical facilities representing benchmark real-world test cases [18].

1.4. Water Gaps in the Reactor Core. The phenomenon considered in this study is related to the presence of water gaps in the reactor core and their local effects. Many reactor designs contain water gaps in the fuel assembly (FA), replacing fuel rods or the core (replacing FAs) to serve various purposes. For example, different types of LWR (e.g., PWR, BWR, and MTR) FAs contain water or void channels for improved or reduced neutron moderation [21]; research reactors often assemble a core with a water gap at the center (thermal flux trap) to irradiate samples [22, 23], and the neutron reflector in many reactors contains water channels for cooling and moderation [24, 25]. Fuel deformation may also lead to water gaps due to either mechanical bowing [26–30] or meltdown during severe core accidents [31, 32].

The presence of water gaps in the core affects its global physical properties, such as kinetic parameters, neutron energy spectrum, excess reactivity, power distribution, and PPF [26, 29, 33–35]. Multigroup diffusion codes (nodal and fine mesh) can predict these well. However, the interfaces between the fuel and the water gap exhibit abrupt and significant local changes in the energy spectrum, burnup, and spatial power distribution. These significant local changes may consequently give rise to large local PPFs, which can only be adequately studied using high-fidelity models. These local effects must be considered in the reactor's nominal operation, and safety analyses should meticulously study and understand this effect.

1.5. Scientific Contribution and Novelty. In this work, a high-fidelity model is developed to study the highly-localized behavior of the neutron flux, energy spectrum, and power distribution in the close vicinity of an interface between the fuel and a flux trap in a thermal reactor core. The model was developed according to an experimental setup designed, built, and used to measure such local effects in the Israeli Research Reactor 1 (IRR1). The local power distribution along a fuel plate adjacent to the flux trap was obtained through a series of measurements, and the model was validated against it.

This study provides in-depth theoretical insights into the feedback mechanism underlying the local PPF. The high level of thermal flux in the flux trap leads to locally increased power density in fuel segments adjacent to the flux trap, leading to increased PPF. However, the increased power density in these segments also induces faster burnup rates, which tends to flatten the power distribution over time and decrease the local PPF. The nonlinear feedback loop between the PPF and the fuel burnup exhibits a trade-off behavior near the flux trap, where higher PPF leads to a faster burnup rate and lower PPF leads to slower burnup. Moreover, in this study, the experimental setup of the core was such that the flux trap was close to partially inserted control rods, enabling the study of the control rods' effect on the PPF near the flux trap.

The highly localized behavior of the PPF and the burnup distribution is studied on a sub-FA neutronic model with a fine-mesh resolution for the power distribution and the fuel burnup. The model enables to obtain qualitative and quantitative results of the PPF and the thermal flux distribution around the flux trap. The results are verified against experimental measurements of the power distribution performed in IRR1.

The results exhibit substantial sensitivity to the model's spatial resolution. Significant differences may arise between the PPF calculated on a sub-FA fine scale and an FA scale. Finally, the experimental verification of the model enables the prediction of the PPF in other regions in the fuel, not accessible to measurement instrumentation, with high confidence.

The novelty of this paper lies in the development of a high-fidelity Monte Carlo model and its utilization to investigate the highly-localized behavior of the PPF within a reactor core, specifically near the interface between the fuel and the flux trap. The impact of flux traps on local power peaking, resulting in a concentrated increase in power density, is examined. The theoretical insights obtained from this study shed light on the feedback mechanism underlying the local PPF. These insights have potential applications in reactor design optimization, operational improvements, and safety margin assessment for reactors sharing similar characteristics, including large light-water power reactors. Furthermore, the experimental validation of the model, which was carried out in an MTR research reactor, enhances the ability to confidently predict the PPF in other FA regions inaccessible to measurement instrumentation.

The paper is organized as follows. Section 2.2 describes the experimental setup in IRR1 and the measurements performed to obtain the power distribution in fuel plates nearing the flux trap. Section 2.3 describes the methodology underlying the development of the computational model. Section 3 describes the results of the experimental

measurements and the computational model simulations, and Section 4 summarizes the conclusions.

2. Methodology

2.1. Methodology Overview. The methodology for investigating the localized behavior of the power peaking factor in a reactor core is described in this section. The methodology is based on two complementary methods. First, the investigation utilizes a high-fidelity Monte Carlo model, which accounts for the influence of flux traps on the local power peaking. The model incorporates a fine spatial mesh to accurately represent the distribution of fission power and burnup. Second, experimental measurements of the power distribution obtained from a specific fuel assembly near the flux trap are used to validate the results obtained from the model.

In this study, the power distribution is inferred from the gamma emission intensity of the fission products along the FA [36–39]. The underlying concept of the experimental measurements is based on the proportionality between the fission power density experienced by the fuel and the concentration of fission products in it. The higher the fission power density, the larger the concentration of fission products and the stronger the gamma emission. Hence, the spatial distribution of gamma emission intensity can serve as a measure of the power density distribution [37, 40].

Hence, to obtain the power distribution in a FA near a flux trap, a suitable FA is chosen and irradiated in a proper location in the core to generate a detectable quantity of fission products. Then, the relative emission intensity of suitable fission products is measured using gamma spectroscopy [40]. The measured fission products should have distinct gamma peaks to identify them in the spectrum and have a half-life of hours to days [36]. Considering a FA that was not irradiated in the core in the months before the experiment, it is assured that all measured fission products were produced during the experimental irradiation, correctly reflecting the power distribution in the experiment.

A dedicated experiment was designed and performed to study the local effect of a flux trap on the PPF. The chosen FA for the experiment possesses two favorable traits. First, it is significantly depleted, where the level of depletion measures the percentage of ^{235}U already consumed within the fuel (for example, 20% depletion means 20% of the initial amount of ^{235}U was consumed). The local depletion in chosen FA ranges from 20% to 80%, and an average depletion of 58% [41, 42], ensuring a distinctive depletion profile of the FA. Second, it was not irradiated in the last decade, allowing the relatively short-lived fission products to decay, reducing the noise level in post-irradiation measurements. The measurement of the long-lived fission products (e.g., ^{137}Cs) enables us to determine the average power distribution experienced by the fuel plates during their irradiation history and, consequently, their depletion [41, 43].

The FA was positioned in the IRR1 core next to a vacant lattice cell filled with water (the flux trap) and was irradiated for three hours with a total core thermal power of 5 MWth. Post-irradiation measurements of the short-lived fission products were used to study the effect of the recent irradiation on the PPF.

A complementary Monte Carlo simulation of the FA irradiation experiment was performed to verify the experimental results and validate the computational model. The model was developed using the continuous-energy Monte Carlo code Serpent [13]. The core model, the calculation scheme, and the simulation parameters are described in Section 2.3.

2.2. The Experimental Setup

2.2.1. IRR1 Specifications. The IRR1 is a 5 MWth pool-type research reactor operating at the Soreq Nuclear Research Center (SNRC) located in Yavne (Israel) for about 60 years. The reactor reached its first criticality in June 1960. It has been operated by the Israel Atomic Energy Commission (IAEC) ever since. The reactor is moderated and cooled by light water. The FAs consist of HEU MTR plate-type fuel elements; each FA contains 23 parallel plates made of highly enriched UAlx-Al fuel (93% 235 U). They are held inside an aluminum casing [41].

Each fuel plate is made of fuel meat coated by aluminum cladding. The pitch dimension is 7.61 cm × 8.0 cm along the x and y axes. The fuel plates are placed in a grid separated by water which provides cooling and moderation. Figures 1(a) and 1(b) show a three-dimensional schematic illustration of an MTR FA and a horizontal (x - y plane) view of the FA from the geometric plots generated by the Serpent code.

The control FAs are similar in geometry to the standard FA but contain 17 fuel plates (three fuel plates are removed from each side, see Figure 2). The space left is used to accommodate the moving control blades. The latter is composed of Ag-Cd-In (80, 5, and 15% wt., respectively) and is shaped as a double-blade fork. The control blades are coated by a thin nickel layer and always move together. In nominal operation, the control blades are usually inserted to about 20-25%, i.e., from $z = 60$ to z = 45 cm.

One of the control FAs does not contain fuel plates. Instead, there is a beryllium block between the control blades, functioning as a neutron reflector and moderator by isotropic elastic scattering. The location of the control blades in the FA is similar to the other control FAs. The beryllium block is rectangular without corners. Instead of each corner, there is a small aluminum rectangular. The entire element is framed with an aluminum frame that holds the structure together (see Figure 2). Other core elements consist of graphite blocks acting as neutron reflectors and moderators.

The FAs are positioned on a grid plate connected to a supporting structure. They are in a 5×5 or 5×6 arrangement, loading 24-30 FAs. Figure 3 shows the core configuration used for this work, where the burnup level in percentage is reported for each FA. Since IRR1 is a research reactor, it operates according to the changing experimental programs; hence, there is no standard or typical core configuration. The main reactor parameters of IRR1 are summarized in Table 1. A comprehensive description of IRR1 technical specifications can be found in Ref. [44] and in Appendix

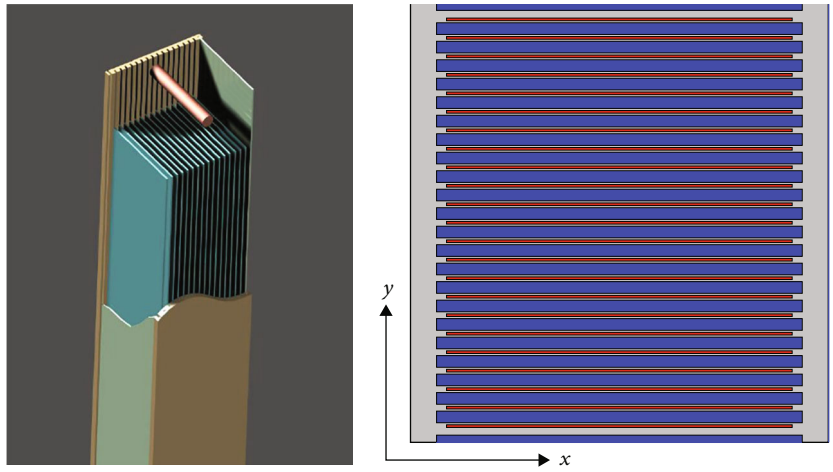

Figure 1: (a) A schematic illustration of a three-dimensional FA axial cut. (b) A horizontal (x - y) view of standard FA plotted by the Serpent model of an IRR1 FA. Blue, light gray, dark gray, and red represent water, cladding, side plates, and fuel meat, respectively.

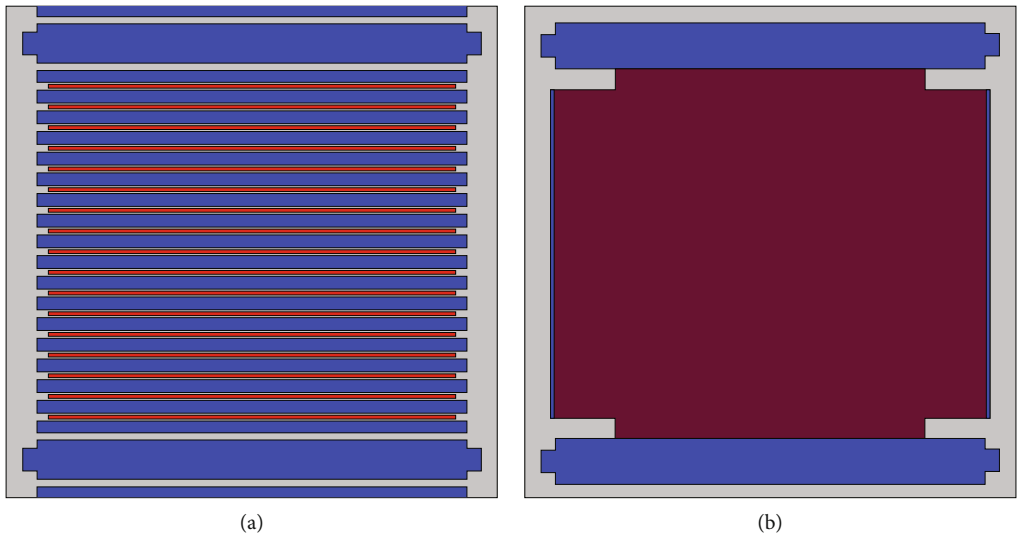

Figure 2: The geometry of regular control FAs (a) and the beryllium control FA (b) without control blades. The beryllium block is marked with dark red. Other colors are the same as in Figure 1.

A, where the material density of each element is given in Table 4, and the geometry of a fuel plate, a control blade, and the beryllium block are given in Figures 16–18, respectively.

2.2.2. Experimental Spectroscopy Measurements. The post-irradiation measurements were performed two weeks after the FA irradiation, using an experimental setup similar to the one described in Ref. [42]. The setup consisted of a high-purity germanium spectroscopic gamma detector (a Canberra Falcon 5000 HPGe detector) aligned with an air-filled collimator positioned above the FA, which was lying horizontally in the pool on a designated stage 2.5 meter below water level, as shown in Figure 4. A motorized stage was used to hold the Ge detector and the collimator and to scan the FA, where the fuel plates are oriented perpendicularly to the collimator, as shown in Figure 4. The fission products' decay counts are assumed to be proportional to the power density that existed in the FA during the last irradiation. They are an excellent indicator of the power density profile and PPF in the irradiated FA.

The FA used for the experiment was 58% depleted on average (see Figure 3), with local depletion ranging from 20% to 80%. It was inserted into the IRR1 core and irradiated next to a flux trap (an empty lattice cell) filled with water, as shown in Figure 3. The FA was irradiated for three hours, with the core operating at a nominal thermal power of 5 MWth. The assembly was then removed from the core for two weeks.

The long-lived isotope ^{137}Cs (half-life of about 30 years) is considered in the analysis as indicative of the entire irradiation history. The short-lived isotopes, such as ^{131}I, ^{132}I,

G	G	G	G	G	G	G	G
G	38%	26%	R	57%	54%	2%	G
G	12%	67%	46%	76%	47%	7%	G
G	22%	39%	53%	50%	55%	11%	G
G	21%	72%	43%	Be	42%	10%	G
G	2%	33%	58%	W	46%	3%	G
G	G	G	G	DFT	G	G	G

(a)

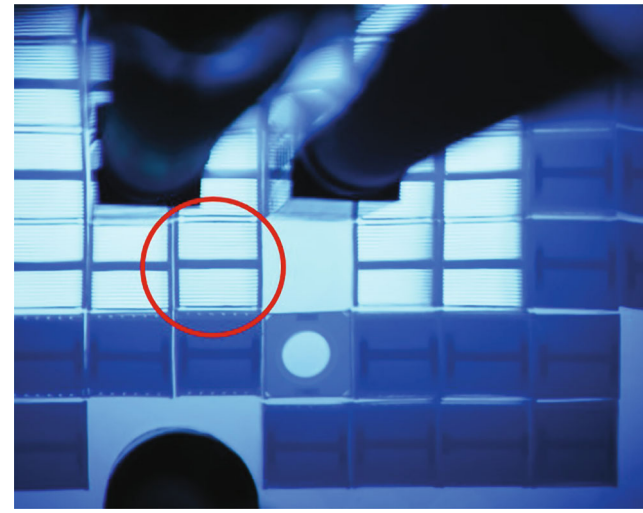

(b)

Figure 3: The IRR1 core configuration used in this study. The percentages indicated mark the depletion of every FA (a). W: water; G: graphite block; Be: beryllium control site; DFT: irradiation channel; R: regulating control rod. Red fill: control FAs; red outline: the FA used in the experimental campaign.

Table 1: Design specifications data of IRR1 located at Soreq NRC [44].

Parameter	Value
Reactor type	Open pool
Thermal power	5 MWth
Maximal neutron flux	$1 \times 10^{14}\ \mathrm{cm}^{-2}s^{-1}$
Fuel type	MTR, flat parallel plates UAlx-Al dispersion, 93% wt.
Active height	60 cm
Coolant	Light water, downward flow
Moderators	Light water
Reflectors	Graphite + light water
FA dimension	$7.61 \times 8.0 \times 87.3\ \mathrm{cm}^3$ (x-y-z)
No. standard FAs	20-26
No. control FAs	3-4 (+one be FA)
Configurations	5×5 or 5×6 or 5×7
Irradiation positions	1-3

^{140}La, and ^{99m}Tc, could only originate from recent irradiation of the FA. The gamma spectroscopy analysis technique was similar to the one used by Mora et al. [45]. Table 2 details the isotopes measured in the experiment.

The two-week waiting period post-irradiation is an optimization between two desired objectives. On the one hand, immediately after irradiation, the activity of the FA is too high, resulting in significant dead time and detector saturation. Consequently, the FPs needed to decay. On the other hand, too long of decay will reduce their activity too much, so the measurement statistics are compromised.

Although ^{132}I, ^{99m}Tc, and ^{140}La have half-lives of several hours to a day, they do not disappear after two weeks. The reason is that these short-lived isotopes are not generated directly from fission. They are mainly generated through the radioactive decay of their parent isotopes, which have much longer half-lives, as indicated in Table 2. The normalized activity of the different FPs is shown in Figure 5 for a single fuel plate of a height of 1 cm that had been irradiated for 1 hour in a power density of 250 W/cm (corresponding to a full-core power of 5 MWth).

Using a high-purity germanium detector, the FA was then scanned along the x-direction at height $z = 56$ cm (4 cm below its top), as shown in Figure 4. The analysis concerns fission products having short half-lives, ensuring that the only contribution measured is of recent irradiation. The gamma spectroscopy results are translated to the power distribution (and the PPF), assuming proportionality between the power density during irradiation and the fission products.

2.3. High-Fidelity Monte Carlo Simulation. A key aspect of this study is the creation of a high-fidelity Monte Carlo simulation of the experimental setup. The purpose of the numerical simulations is twofold. First, the validation and verification of the model and experimental procedure are achieved through a comparison of experimental measurements with numerical simulations, thereby increasing their reliability. Second, the experimental verification of the model allows for accurate prediction of the PPF in regions of the FA that are not accessible to measurement instrumentation.

2.3.1. The Minicore Model. The Monte Carlo simulation involves a three-dimensional model of the relevant portion of the IRR1 core, using both the original design specification and the experimental setup design. The core configuration and fuel composition (i.e., its depletion level) are based on the time at which the experiment was performed, as provided by the reactor operator.

Table 2: The isotopes measured after the FA irradiation [46].

Isotope	Half-life	Parent-daughter decay chain	Fission yield* (%)	Spectral line (keV)
^{137}Cs	30.08 y	$^{137}\text{Xe} \xrightarrow[3.8\ \text{min}]{\beta^-} {}^{137}\text{Cs}$	6.221	662
^{140}La	1.679 d	$^{140}\text{Ba} \xrightarrow[12.75\,\text{d}]{\beta^-} {}^{140}\text{La}$	6.315	487, 1596
^{131}I	8.025 d	$^{131}\text{Te} \xrightarrow[25\ \text{min}]{\beta^-} {}^{131}\text{I}$	2.878	364
^{132}I	2.295 h	$^{132}\text{Te} \xrightarrow[77\,\text{h}]{\beta^-} {}^{132}\text{I}$	4.295	668
^{99m}Tc	6.007 h	$^{99}\text{Mo} \xrightarrow[66\,\text{h}]{\beta^-} {}^{99m}\text{Tc}$	5.400	140

* Cumulative fission yields per thermal fission of ^{235}U [%].

Table 3: Calculated PPF values at different heights.

Height	Parameter	PPF	Average PPF
$z = 56$ cm	Upper plate	1.122 ± 0.010	1.254 ± 0.009
	Middle plate	1.477 ± 0.010	
	Bottom plate	1.168 ± 0.008	
$z = 30$ cm	Upper plate	1.551 ± 0.009	1.482 ± 0.008
	Middle plate	1.642 ± 0.011	
	Bottom plate	1.281 ± 0.010	

The model is created using the Serpent code [13] with the JEFF-3.1.1 evaluated nuclear data files [47] and represents a part of the core, referred to as a "minicore," which includes the 3×3 elements surrounding the FA of interest. The minicore configuration is depicted in Figure 6. As shown in this figure, the four fuel assemblies (three standard and one control) have different depletion levels. While the depletion levels were given by the reactor operator, the corresponding material and isotopic composition of the fuel were determined for each depletion level using the computational procedure described below.

The minicore's size was determined by considering the FAs and the neutron flux that might influence the local power distribution in the central FA. In light water, the mean free path (mfp) of thermal neutrons is on the order of a few millimeters [48], while the size of an FA, measuring $7.61 \times 8.0\,\text{cm}^2$, corresponds to many mean free paths of thermal neutrons. Consequently, neutrons or other components located further away, i.e., outside the minicore, are likely to have a weak influence on the neutron flux and the power peaking at the central FA and its interface with the flux trap. These external effects can be regarded as second-order effects, with the dominant contributions arising from the neutron interactions and flux within the minicore region.

In what follows, the terms upper, middle, and bottom plates refer to the fuel plates' location inside the central FA in the horizontal (x-y) plane, as depicted in Figure 6. The term "top" refers to higher values along the z -axis.

2.3.2. The Calculation Scheme. An independent burnup calculation is performed for each FA until it reaches the designated average level of depletion according to its documented burnup history. The single FA burnup calculation model divides every FA's top, middle, and bottom plates into 30 horizontal (x) and three axial (z) regions (a total of 90 burnup regions). Reflective boundary conditions are imposed in the horizontal direction representing an infinite lattice. Along the z-axis, the upper 30 cm water volume and lower 15.72 cm support grid are modeled.

The material compositions of each depleted FA are imported into the minicore model, shown on the right of Figure 6. Note that the minicore model is highly heterogeneous due to the flux trap, the irradiation channel, the graphite, the beryllium block, and the different depletion levels of the FAs. In the minicore model, void boundary conditions are used in the x-y plane.

Finally, the minicore model is used to obtain the flux and the power distribution in the central FA. Similarly to the FA burnup calculations, the upper water volume and the supporting grid block are modeled for the minicore model. A total of 125 million neutron histories are used for each minicore calculation (1,250 active and 60 inactive cycles with 100,000 particles per cycle), yielding a statistical uncertainty of a few tens of pcm in keff.

2.3.3. The Partially Inserted Control Rods. IRR1 is routinely operated with the control rods partially inserted into the upper part of the core to about 25% depth [41, 42]. This translates into the upper 15 cm of the fuel's active zone. Since the control rods significantly affect the neutron flux spectrum and spatial distribution, they must be considered in the simulation model. The partial insertion of the control rods is demonstrated in Figure 7, where a horizontal cross-section of the minicore is shown at different heights (height is measured upwards from the bottom part of the fuel's active region). At $z = 56$ cm (Figure 7(a)), the control rods are visible in the top right and left FAs (marked in yellow). However, below $z = 45$ cm, no control rods are present, as shown for $z = 30$ cm (Figure 7(b)).

3. Results and Discussion

3.1. Simulation Results. The power distribution within the fuel volume was quantified for the top, middle, and bottom plates (as depicted in Figure 6). The horizontal and axial

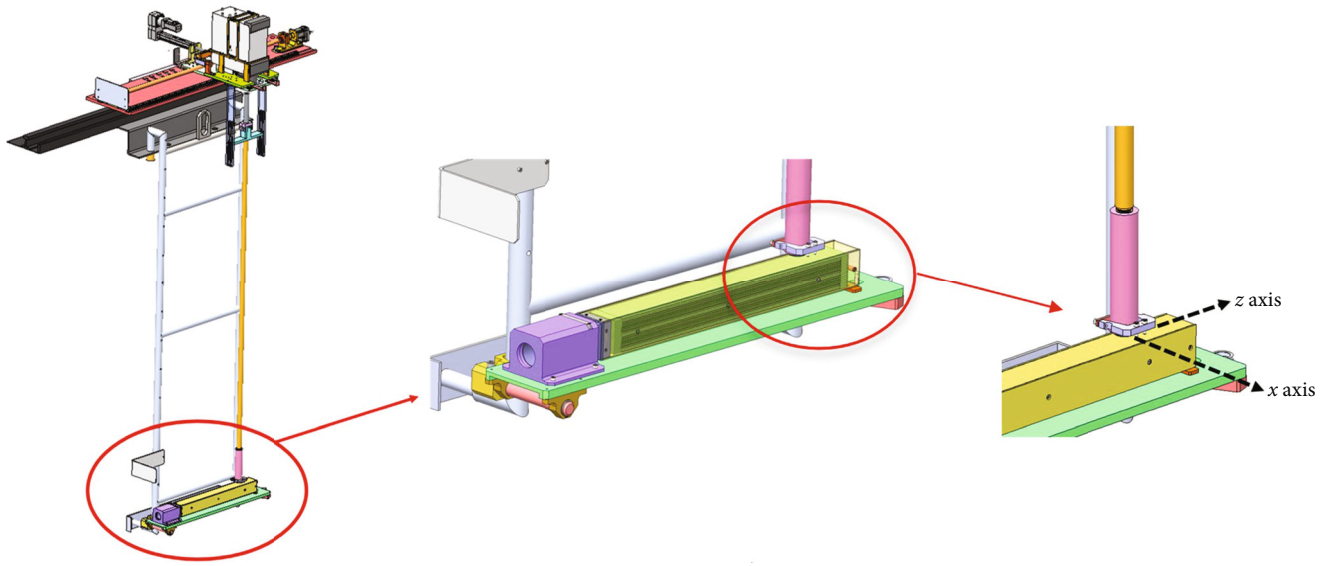

Figure 4: The experimental setup consisted of a high-purity germanium spectroscopic gamma detector mounted on a motorized stage above the water level, aligned with an air-filled collimator positioned above the FA, which was lying horizontally on a second designated stage inside the pool. The fuel plates were oriented perpendicularly to the collimator.

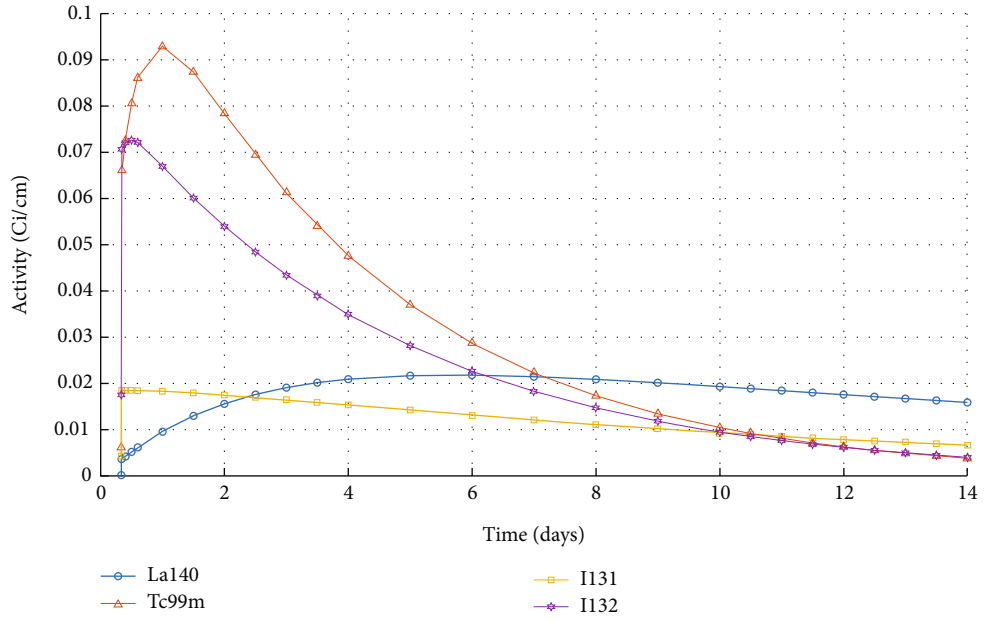

Figure 5: The normalized activities of the different FPs for a single fuel plate of a height of 1 cm that had been irradiated for 1 hour in a power density of 250 W/cm, corresponding to a full-core power of 5 MWth.

power density distribution was subsequently analyzed, and the local PPF was calculated at various axial positions.

3.1.1. Horizontal Power Distribution. The mesh plots produced by Serpent, which depict the thermal flux and fission density distributions, serve as a useful tool for illustrating the neutronic behavior of the system and gaining qualitative insights. As an example, Figure 8 presents horizontal cross-sections of the thermal flux and fission power distributions at two axial positions: $z = 56$ cm and $z = 30$ cm. These cross-sections correspond to the locations depicted in Figure 7.

Several qualitative observations can be made based on the information provided in Figures 8 and 9, which is a zoom-in on the central FA. Specifically, at the midheight of the fuel assembly ($z = 30$ cm), there is a notable difference in power distribution between the edges of the plates closer to the water gap and beryllium reflector compared to the remaining plates that are farther away. Similarly, elevated power levels are observed in the plates facing the graphite

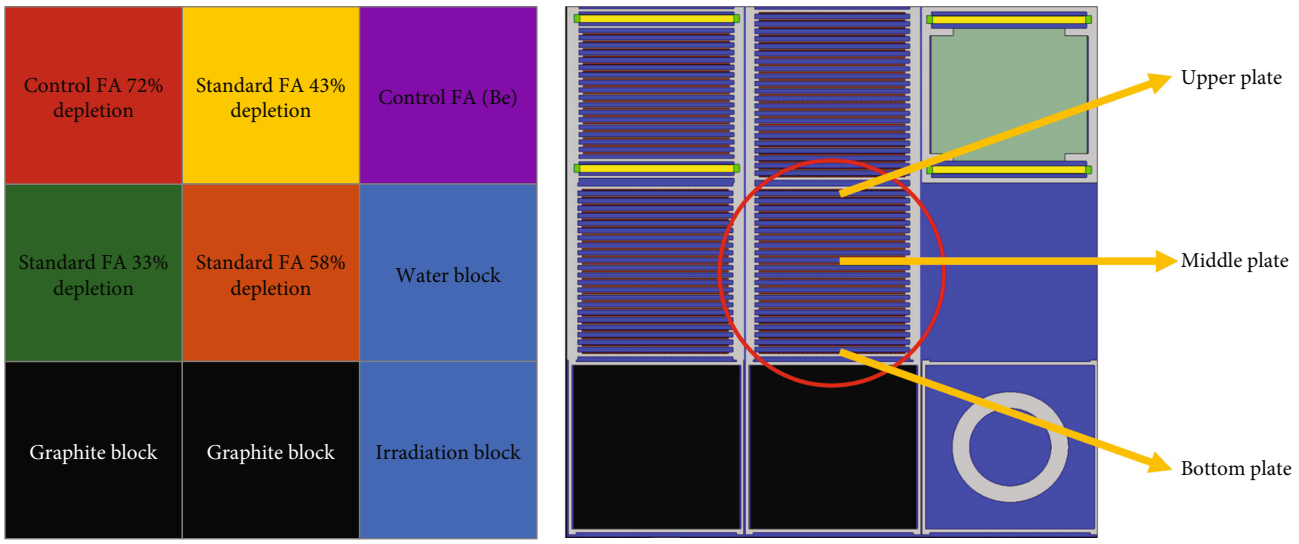

FIGURE 6: (a) The minicore configuration. (b) Horizontal cross-section of the minicore Serpent model, where the plate orientation is clearly visible. The Al-In-Cd control rods are marked in yellow. Assuming this selection affects only the minicore's peripheral region but not the spectrum or flux distribution in the FA of interest.

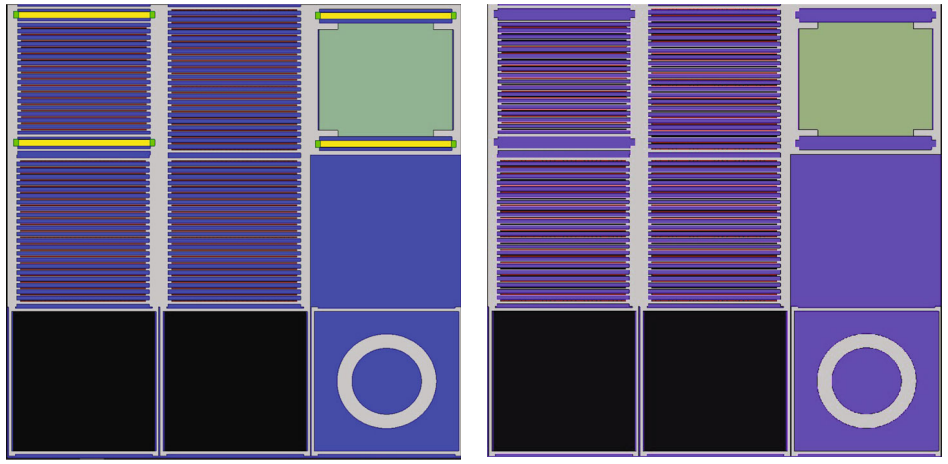

FIGURE 7: A horizontal cross-section of the minicore at different heights. At $z = 56$ cm (a), the control rods are visible in the top right and left FAs (marked in yellow). At $z = 30$ cm (b), however, no control rods are present.

reflector and those near the empty control channels. If this observation is not clearly noticeable in Figure 8, the reader is referred to Figures 9 and 10. This increase in power can be attributed to the accumulation of thermal flux in the vicinity of the water gaps and the reflector.

At this specific height within the fuel assembly, the impact of the control rods on the flux distribution is minimal compared to the influence exerted by the water gaps and graphite reflectors. The accumulation of thermal flux near the water gaps and reflector leads to a localized increase in power density, resulting in the observed elevated power levels in the mentioned regions of the fuel assembly.

An increase in the thermal neutron flux leads to an increased fission rate in the fuel due to the fundamental nature of nuclear fission reactions, i.e., the high fission cross-section of thermal neutrons compared to fast ones. The fission rate at any point $\mathbf{r}$ in the fuel is proportional to the multiplication of the neutron flux and the macroscopic fission cross-section, i.e., $\sim \int dE\Sigma(\mathbf{r}, E)\phi(\mathbf{r}, E)$. Hence, a softer spectrum at point $\mathbf{r}$ locally increases the contribution of thermal fissions, resulting in increased local power.

In the upper part of the fuel assembly, specifically at the height of $z = 56$ cm (4 cm below the top end of the fuel plate), Figure 8 shows an increase in power near the flux trap and the graphite reflector. However, in contrast, the power levels near the control rods are significantly reduced. This power distribution discrepancy arises from a thermal flux deficiency caused by increased absorption within the control rods.

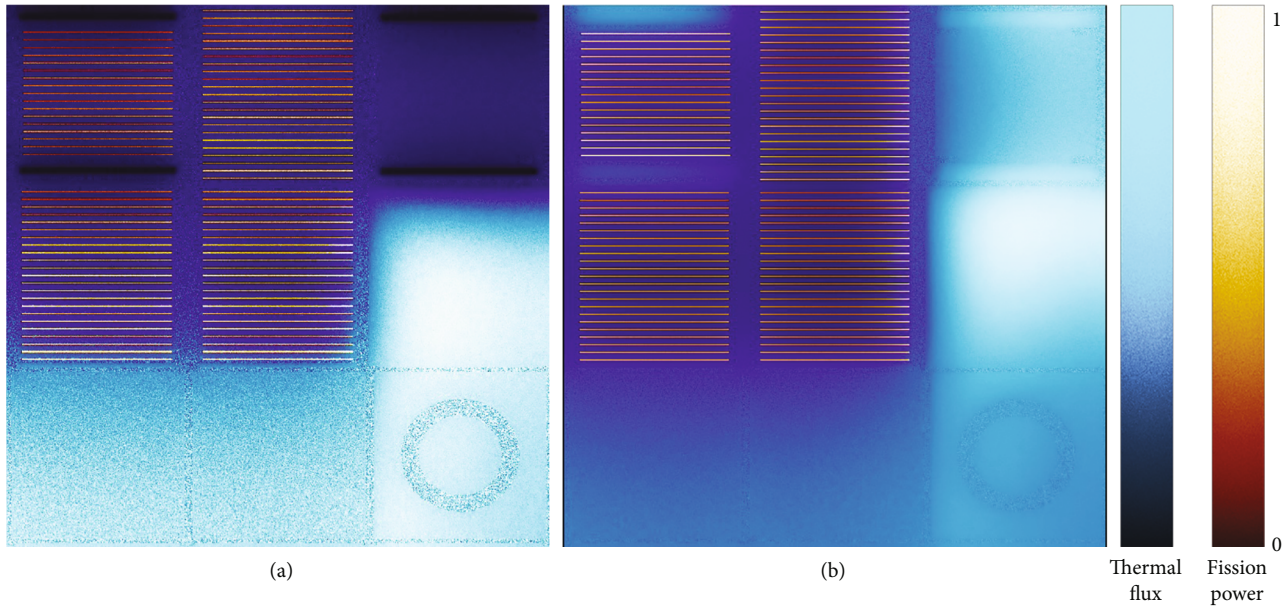

Figure 8: Horizontal cross-sections of the thermal flux and fission rate distributions at two different heights, $z = 56$ cm (a) and $z = 30$ cm (b). The control rods are evident at $z = 56$, but they do not reach $z = 30$. Hot and cool shades represent the relative fission power and thermal flux distributions, respectively, where brighter shades indicate higher values. (a) The black areas at the top of the plot indicate the presence of the control rods (blade-shaped), leading to vanishing thermal flux values.

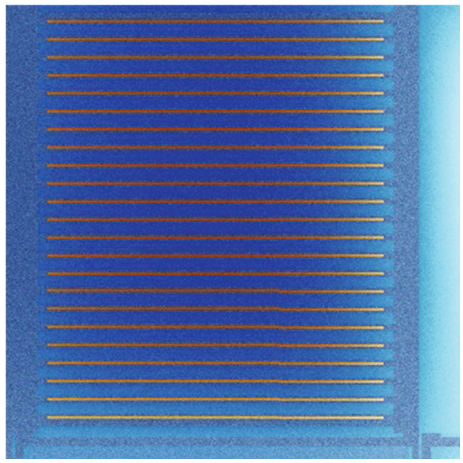

Figure 9: A zoom-in on the central FA in Figure 8 at $z = 30$ cm. A horizontal cross-section of the thermal flux and fission rate distributions. Hot and cool shades represent the relative fission power and thermal flux distributions, respectively, where brighter shades indicate higher values. The reader may refer to the color bar in Figure 8.

The control rods, designed to regulate the nuclear reaction, possess a high capacity for neutron absorption. As a result, they reduce the thermal neutron flux available for fission reactions in their vicinity. This reduced availability of thermal neutrons leads to decreased power density near the control rods.

Consequently, in this experimental setup, the proximity to the control rods is expected to influence the local PPF notably. The deficiency in thermal flux caused by increased absorption in the control rods affects the power distribution, resulting in lower power levels near the control rods compared to the regions near the flux trap and graphite reflector.

Figure 8 demonstrates that at $z = 56$ cm, the impact of the control rods on the power distribution is particularly significant on the upper fuel plate compared to the middle and bottom plates. As a result, the power distribution along the upper plate is expected to be more uniform or flatter than the middle plate.

The reason for this flattening effect is attributed to the proximity of the upper plate to a strong and spatially extended neutron absorber, which refers to the control rods in this context. The presence of the control rods acts as a substantial neutron absorber, leading to a reduction in the spatial variations of the power distribution. Consequently, any strong localized variations in power are smoothed out, resulting in a relatively more uniform power distribution along the upper plate.

Similarly, the bottom plate is influenced by its proximity to the graphite reflector, which also leads to a flattening effect on the power distribution (this effect is clearly visible in Figure 10). The graphite reflector serves as a neutron diffuser, spreading the neutron flux more evenly across the bottom plate. This diffusing effect mitigates pronounced spatial variations in power, leading to a flatter power distribution along the bottom plate.

Therefore, both the upper plate's proximity to the control rods and the bottom plate's proximity to the graphite reflector contribute to a more uniform power distribution, smoothing out significant spatial variations in power along these plates.

During the neutron transport calculation, the power density at the upper part of the fuel plate, specifically around $z = 56$ cm, was evaluated using a specific voxel configuration.

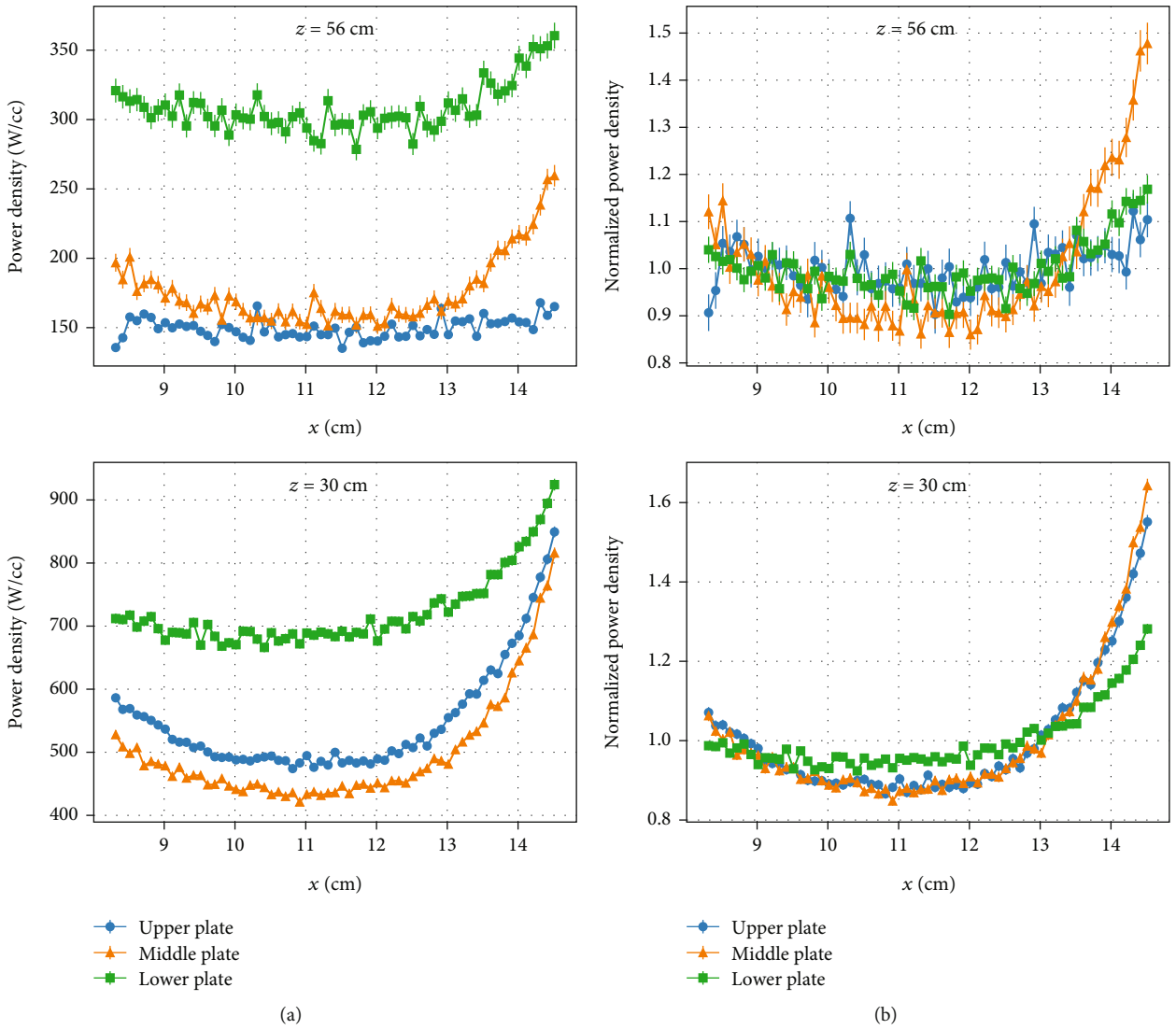

FIGURE 10: The calculated power distribution along the x-axis within the fuel plates at different heights ($z = 30$ cm and $z = 56$ cm), with the absolute (a) and normalized (b) values. The error bars at $z = 30$ cm are hardly visible because their size is smaller than the marker size.

This configuration involved dividing the upper 8 cm of the fuel plate into 64 voxels (regions) along the x-axis. Each voxel had dimensions of 0.1 cm in the x-direction, 0.051 cm in the y-direction, and 8 cm in the z-direction.

A similar voxel configuration in the x- and y-directions was employed to determine the power density at the plate's midheight but with a voxel height of 20 cm (not 8 cm) in the z-direction. These voxels were positioned within the plate between the heights of $z = 20$ and $z = 40$ cm.

By employing these voxel configurations, the power density at different heights along the x-axis of the plate was obtained. The resulting power density values were then plotted against the x-axis at various heights, as depicted in Figure 10. This approach allowed for detailed visualization of the power distribution along the x-axis at different heights within the fuel plate, providing valuable insights into the spatial variations of the power density in the specified regions.

The qualitative effects discussed previously, as depicted in the mesh plots, are now examined quantitatively. The power density at the midheight of the FA is higher compared to the upper part, which is closer to the control rods. The elevated power density near the flux trap is moderated by the control rods at the upper part of the FA compared to the power elevation at midheight.

The bottom plate, which is closer to the graphite reflector, exhibits higher power density along the entire x-direction compared to the middle and upper plates at any height. However, the power increase towards the flux trap is moderated due to the strong effect of the graphite reflector and the accumulation of thermal neutrons around this plate.

The middle plate, which is farther away from the graphite reflector and the control rods (compared to the upper and bottom plates), exhibits a significant power increase near the flux trap at all heights. The upper plate exhibits similar behavior to the middle plate, except at the top end of the

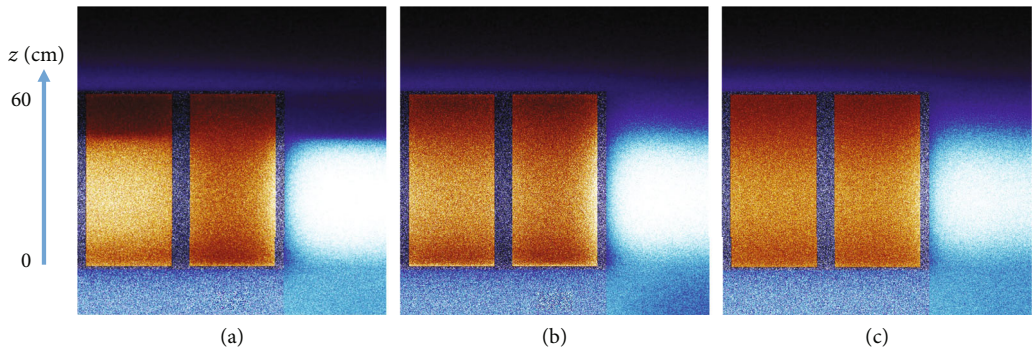

Figure 11: Axial cross-sections of the thermal flux and fission power distributions at three different lateral (x-z) positions corresponding to the upper, middle, and bottom fuel plates, as shown in Figure 6. Hot and cool shades represent the relative fission power and thermal flux distributions, respectively, where brighter shades indicate higher values. The black areas indicate a vanishing thermal flux value. The x and z axes are not to scale (the length of the plate along the x-axis is 7.61 cm, whereas its height is 60 cm). The reader may refer to the color bar in Figure 8. (a) Upper plate. (b) Middle plate. (c) Bottom plate.

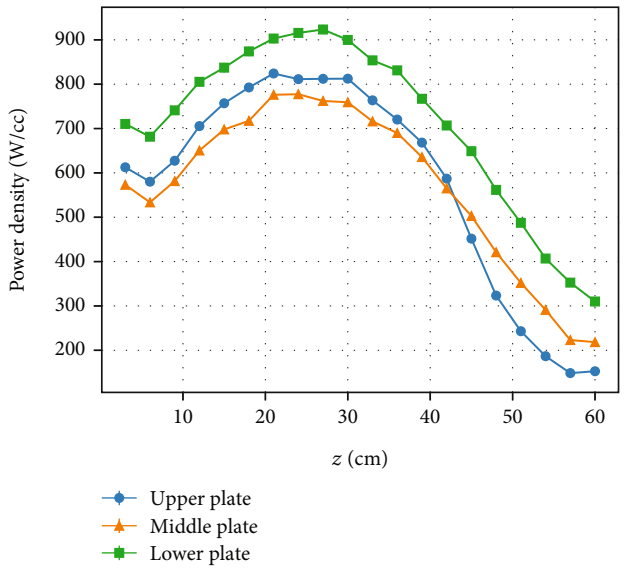

Figure 12: Comparison between the axial distribution of the power density in the upper, middle, and bottom fuel plates.

FA, where the control rods suppress the total power level in the plate and eliminate any power increase near the flux trap.

All plates exhibit a power increase towards the opposite direction from the flux trap, i.e., towards the adjacent FA from the left. This is due to the much lower depletion of this adjacent FA (33%) compared to the central FA (58%). However, this is not true for the upper plate at the upper part of the FA due to the effect of the other control rods from the left.

One can determine the local PPF by analyzing the normalized power density distributions represented in Figure 10. This metric is defined as the ratio between the maximum power value and the average power along the x -axis at a specific height. In a normalized power plot, where the average power along the x-axis is equal to one by definition, the local PPF corresponds to the maximum power value. The highest power value is typically observed near the flux trap, located on the right side of the power distributions displayed in Figure 10.

The statistical errors depicted in Figure 10 are inversely proportional to the power density in the FA. The statistical errors are smaller at the midheight of the FA ($z = 30$ cm), where the power is larger, compared to the upper part ($z = 56$ cm), where the power is lower. The presence of the control rods and axial leakage at the upper part of the FA reduces the neutron density, leading to a decrease in power and an increase in statistical error in that region.

3.1.2. Axial Power Distribution. In Figure 11, the axial cross-sections (in the x-z plane) of the thermal flux and fission power distributions are presented at three different lateral positions corresponding to the upper, middle, and bottom fuel plates, as shown in Figure 6. These plots, which depict the neutron flux and power distribution in the vicinity of a flux trap, illustrate the mechanism that leads to increased values of local PPF. Note that the x and z axes are not to scale (the length of the plate along the x-axis is 7.61 cm, whereas its height is 60 cm).

The influence of the control rods and the graphite reflector on the different plates within the FA can be observed and characterized. The upper plate, being closer to the control rods, experiences a more significant impact than the other two plates.

As the control rods are inserted into the core, they absorb neutrons, reducing the local power density near them. This effect is more pronounced on the upper plate due to its proximity to the control rods. However, as we move towards the middle of the fuel assembly, this impact becomes less pronounced, suggesting a gradual decrease in the influence of the control rods on the power distribution.

On the other hand, the bottom plate is influenced by the presence of the graphite reflector. The graphite reflector acts as a neutron moderator and diffuser, slowing down fast neutrons and increasing the thermal neutron population near the flux trap at midheight. This moderated rise in power density near the flux trap is observed in the bottom plate. The graphite reflector contributes to a more uniform power

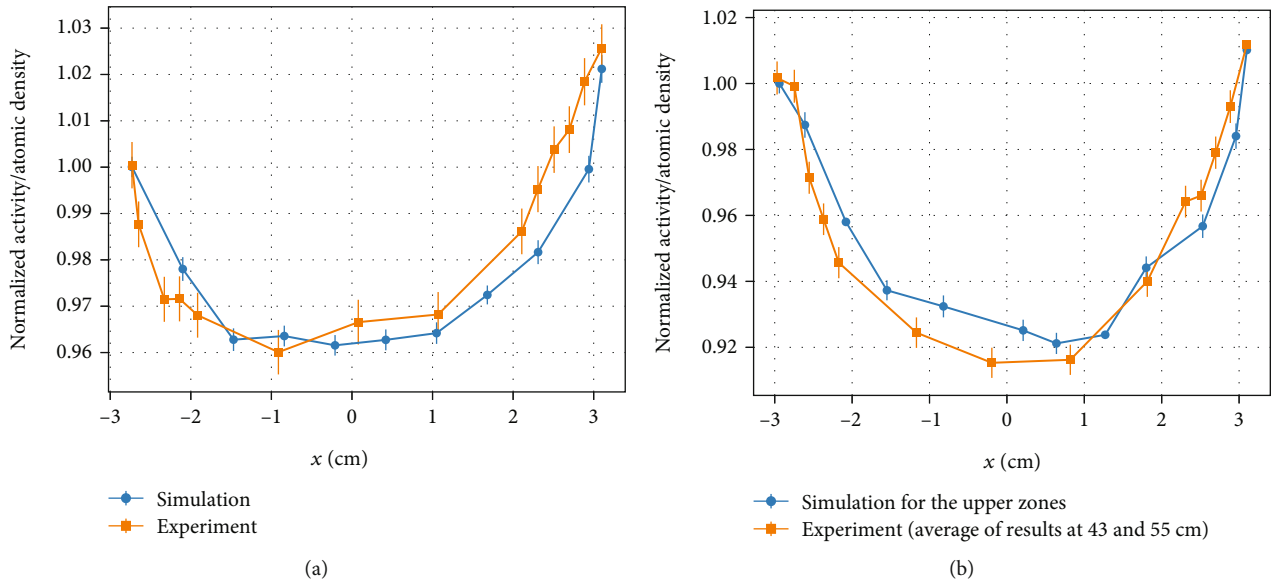

FIGURE 13: Comparison between the measured ^{137}Cs activity and its simulated atomic density along the x-direction at the middle (a) and upper (b) regions of the FA. The different regions (heights) correspond to different depletion values. Both the measured activity and the calculated atomic density of ^{137}Cs are normalized such that the leftmost value equals unity.

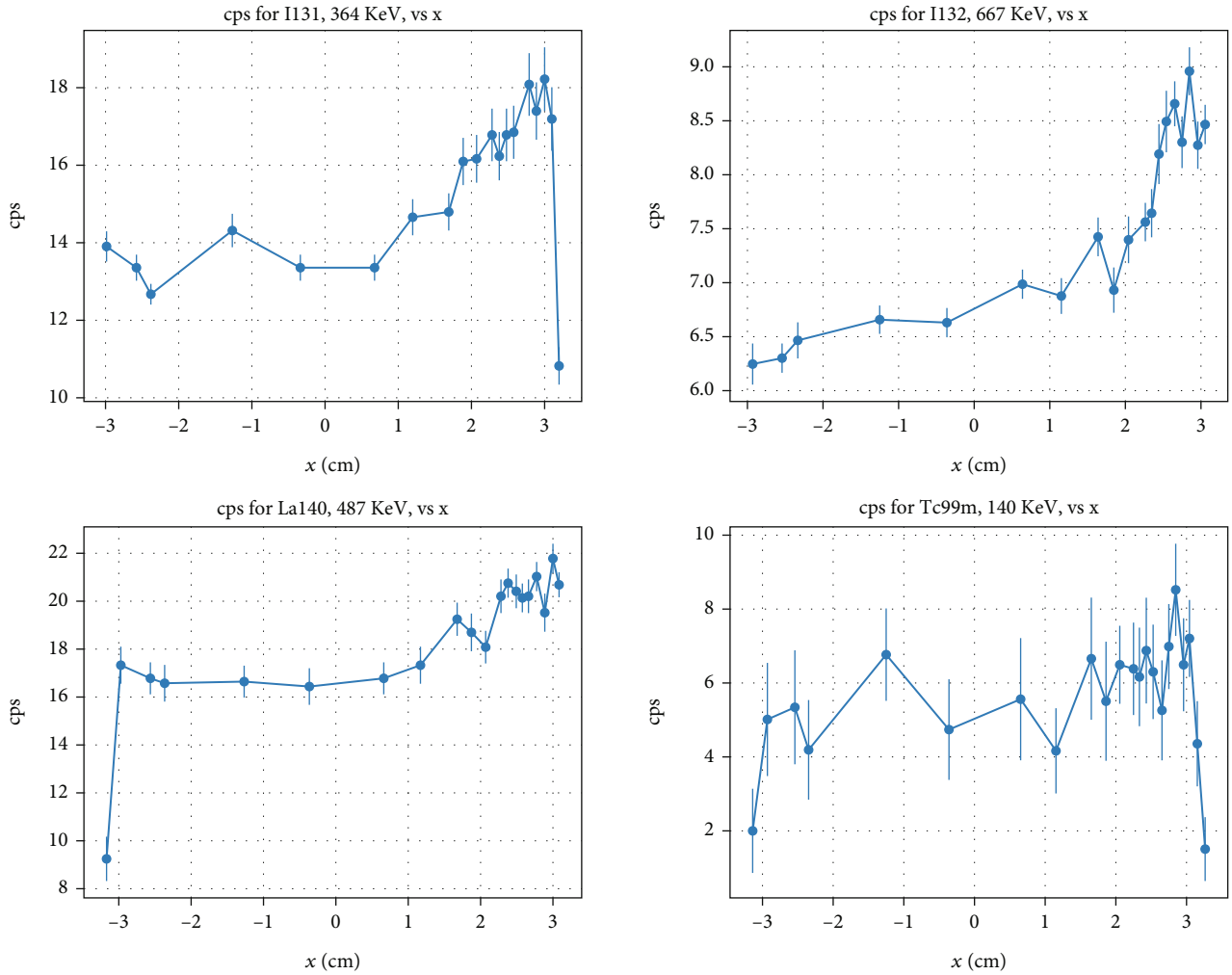

FIGURE 14: Measurement results for several short-lived isotopes.

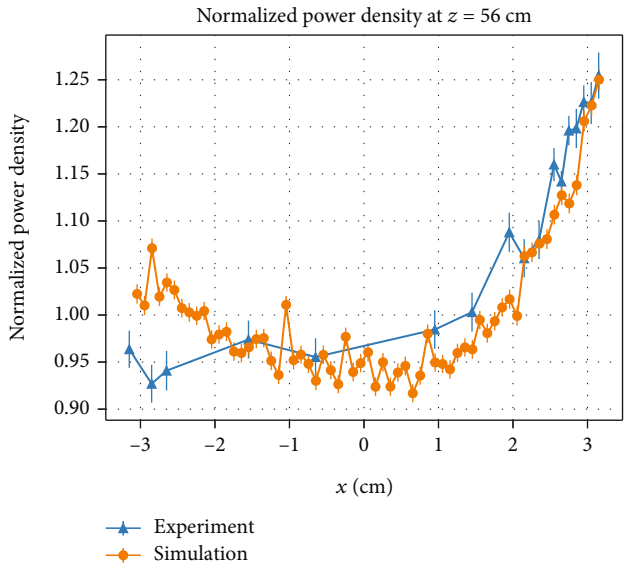

FIGURE 15: A comparison between the measured and calculated normalized power density distribution at $z = 56$ cm. The simulation curve represents an average of the power distribution in the three fuel plates—upper, middle, and bottom (see Figure 6) at $z = 56$ cm.

distribution across the bottom plate than the upper and middle plates.

Regarding power density distribution, the middle and upper plates exhibit a strong peak near the flux trap at midheight. This indicates a localized concentration of power in these regions, likely influenced by the geometrical configuration and neutron moderation effects within the fuel assembly.

The axial power density distribution within the fuel plates was determined by dividing each fuel plate into 20 voxels along the z-axis, with dimensions of 6.4 cm in the x-direction, 0.051 cm in the y-direction, and 3 cm in the z-direction. The resulting power density is plotted along the z-axis for the three fuel plates in Figure 12.

The power density in the bottom plate is the highest along the entire fuel region due to its proximity to the graphite reflector. At the midheight of the FA, where the influence of the control rods is weaker, the power density in the upper plate is greater than that in the middle plate. This is due to the presence of a FA with higher uranium content near the upper plate (43% depletion vs. 58% in the central FA) and the effect of the control rods, which "push" the power downwards in order to maintain a constant power in the core. In contrast, at the upper part of the FA, the proximity of the upper plate to the control rods results in a reversal of this trend.

3.2. Experimental Results

3.2.1. Cumulative Irradiation History Measurement. The measurement of the activity and spatial distribution of the long-lived fission product ^{137}Cs can provide information about the power distribution experienced by the FAs during their irradiation history. This is because the local depletion level is proportional to the cumulative local power, and the measurement of ^{137}Cs can indicate the depletion distribution.

To measure the ^{137}Cs in the FA, a spectroscopy measurement was conducted on the 662 keV emission line of the isotope. It is important to note that the ^{137}Cs measurement was conducted after the FA was cooled outside the core for the past ten years and before its reirradiation near the flux trap. The FA was scanned along the x-axis in three different axial positions, and it was also rotated 180 degrees around the z-axis to measure the plates from the opposite side.

The local depletion level was inferred from the measurements by employing an established methodology [41, 43, 45], assuming that the count rate is proportional to the concentration of the fission product indicator (^{137}Cs in this example). The relation between the count rate and the concentration of ^{137}Cs is described briefly. The number of ^{235}U nuclei that underwent fission, N_f, can be expressed as $N_f = N_i \cdot f/Y_i$, where N_i is the number density of the fission product indicator, Y_i is its fission yield, and f is the decay-buildup correction factor accounting for the intermittent irradiation and cooling periods [43]. The quantity N_i is determined by measuring the activity of the FP indicator given by $N_i = A_i \exp(\lambda_i t_c)/\lambda_i$, where λ_i and A_i are the FP indicator decay constant and activity, respectively, and t_c is the last cooling duration. Finally, the activity is evaluated from the measurement according to $A = R_i/Q_i \cdot \epsilon$, where R_i is the ratio between the net photopeak area of the FP's gamma-ray and the measured count rate, Q_i is the gamma-ray emission probability, and ϵ is the detection efficiency. According to this analysis, the FAs, on average, self-absorb 40% of the gamma rays emitted by ^{137}Cs. The actual measurement is then a weighted average over all the plates. The measured results are compared to the simulation results, as shown in Figure 13.

The simulation results were obtained by performing burnup calculations as described in Section 2.3.2. The FA was burned up to 58% using a fine mesh of 30 cells (burnup zones) of 2 cm width each along the x-axis for the upper, middle, and bottom fuel plates. The simulation was performed with the Serpent code.

The measured concentration profile of ^{137}Cs (Figure 13) suggests that the FA has experienced a relatively homogeneous irradiation history. The profile exhibits a maximal PPF of 1.1, with a hotspot located at $z = 56$ cm and a rather symmetrical power density distribution around the center of the fuel plates in the x-direction. Despite being irradiated in various core positions and in close proximity to other FAs and control rods, the long irradiation history of over 30 years has resulted in a power profile that is representative of uniform irradiation. This suggests that the many heterogeneities present during the irradiation process have been "averaged out" over time.

3.2.2. Measurements of the Flux Trap Effect. The measured short-lived isotopes are detailed in Table 2, and the

measurements' results are presented in Figure 14. The measurements took place at $z = 56$ cm, and scanning was made along the x-axis of the FA.

It is important to note that even though ^{132}I, ^{99m}Tc, and ^{140}La have relatively short half-lives spanning from several hours to a day, they do not entirely decay away within a two-week timeframe. This is because these short-lived isotopes are primarily generated in the fuel through the decay of their parent isotopes rather than directly from fission events, as indicated in Table 2. The parent isotopes, such as ^{99}Mo and ^{132}Te, possess half-lives ranging from 66 to 77 hours, while ^{140}Ba has a half-life of 12.75 days. As a result, the presence of these parent isotopes continues to contribute to the production of ^{132}I, ^{99m}Tc, and ^{140}La, even after the initial two-week period.

In order to decrease the measurement errors, a strategy of combining the results of multiple isotopes measured at the same position was employed. Specifically, the measurement results of the ith isotope at measurement point j, denoted by $y_i(x_j)$, were normalized by their average over N isotopes, and the standard deviation was derived by standard statistical analysis.

Subsequently, a variance-weighted average was performed over the isotopes to obtain the count value, $\bar{y}(x_j)$,

$$\bar{y}(x_j) = \frac{\sum_{i=1}^{N} \left(y_i(x_j)/\sigma_i(x_j) \right)}{\sum_{i=1}^{N} \left(1/\sigma_i(x_j) \right)}. \quad (1)$$

This process was carried out for each measurement position, yielding the measured power density distribution along the x-axis.

The measured experimental values were compared to simulations that evaluated the power density distribution along the same direction (x-axis), with the results normalized to their average. The comparison is depicted in Figure 15, where the simulation curve is an average of the power distribution in the three fuel plates—upper, middle, and bottom (see Figure 6) at $z = 56$ cm. The simulation model utilized for assessing the power density distribution was similar to the one detailed in Section 3.1.1, which was employed for calculating the horizontal power density distribution.

To evaluate the power density, a voxel-based approach was adopted. Specifically, around $z = 56$ cm, the region of interest was divided into 64 voxels along the x-axis, each with dimensions of $0.1 \times 0.051 \times 8\,\text{cm}^3$. Dedicated computational detectors, available in the Serpent code, were utilized to tally the fission rate within each voxel.

The measured and average calculated power density distributions, as illustrated in Figure 15, exhibit similar trends. The power density increases towards the flux trap and peaks at a position closer to it, specifically to the right side of the graph (at $x > 3$).

As previously discussed in earlier sections, this observed trend can be attributed to the accumulation of thermal flux in the flux trap, leading to an increased fission rate near the fuel-flux trap interface. The derived measured and simulated PPF values, corresponding to the maximum normalized power density (to the right of the plot), yield very close results (shown with additional results in Table 3), validating the simulation methodology presented in this study.

Table 4: Material density.

Material	Isotope	Atom density (#/cm-b)
Fuel	U-235	$1.630E-3$
	U-238	$1.211E-4$
Water	H-1	$6.663E-2$
	O-16	$3.331E-2$
Clad (Al)	Al-27	0.271
Absorber	Ag	$4.160E-2$
	Cd	$2.850E-3$
	In	$7.000E-3$
Beryllium	Be-9	0.12
	O-16	$1.38E-3$
Graphite	C-12	$8.03E-2$

3.3. PPF Calculation. In order to validate our model with the experimental results obtained from the aforementioned experiment, the PPF was calculated at the point where the gamma spectroscopy was conducted, i.e., at $z = 56$ cm. The PPF was first calculated for the top, middle, and bottom plates individually, and then an average PPF across all 23 plates in the FA was determined.

To further expand the scope of our study, the PPF was also calculated for all plates at the height of 30 cm in order to assess the effect of the flux trap in a region that is farther from the control rods and the graphite reflector. The results of this analysis are provided in Table 3.

The calculated average PPF value at the experiment height is 1.254 ± 0.009, in good agreement with the measured value of 1.25 ± 0.03, as shown in Figure 15.

4. Conclusions

In this study, the localized behavior of the PPF in a reactor core was investigated using a high-fidelity Monte Carlo model. The effect of water gaps, also known as flux traps, on the local power peaking, was analyzed. The results obtained from the model were validated through comparison with experimental measurements of the power distribution obtained from the IRR1 facility.

The results obtained from the study demonstrated a strong dependence of the local power distribution and PPF on the model's fidelity and the three-dimensional core geometry in the vicinity of the points at which the measurements took place. Significant differences were observed between the PPF calculated on a fine scale as opposed to that calculated at the plate or assembly scale (see Table 3). The calculated PPF at the FA scale was 1.254 ± 0.009 at height $z = 56$ cm (see Figure 15, which is in good agreement with the measured values of 1.25 ± 0.03 performed at the same height.

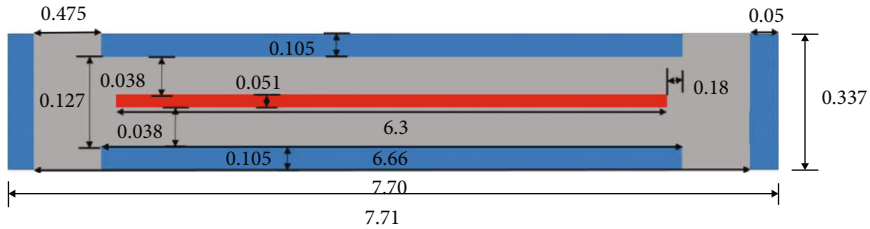

Figure 16: Geometry of a single fuel plate. Blue, gray, and red represent water, aluminum, and fuel meet, respectively. All dimensions are given in cm.

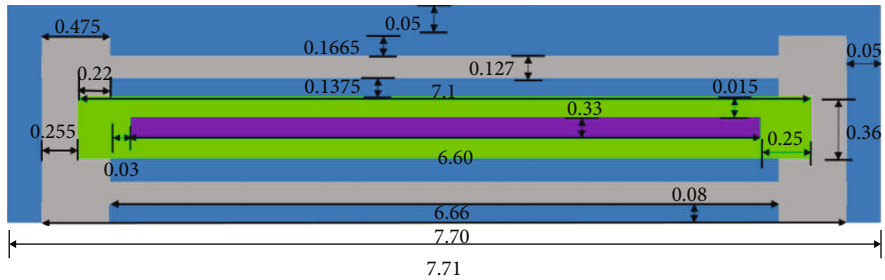

Figure 17: Geometry of a single absorber blade. Blue and gray represent water and aluminum, respectively. Bright green and purple represent the nickel coating and the absorber meat, respectively. All dimensions are given in cm.

Note, however, that at height $z = 30$ cm, where no measurements were performed, the calculated PPF based on the high-fidelity model yielded much higher values, exceeding 1.6. This prediction raises the need for further measurement to validate this value.

The results of this study indicate significant discrepancies between the detailed fine mesh and the average results, as shown in Table 3. For example, the fine-mesh results give a PPF range between 1.122 (upper plate) and 1.477 (middle plate) at $z = 56$ cm, with an average of 1.254. This discrepancy is even more pronounced at $z = 30$ cm, where the maximal local PPF is 1.642, with an average of 1.482. These discrepancies are not conservative because they suggest the actual PPF may be larger than anticipated if using a coarse-mesh or average approach. A high-fidelity model is necessary to account for this localized behavior accurately. This highlights the importance of considering the fine-scale behavior of the PPF in the design and operation of nuclear reactors to enable performance optimization while ensuring safety.

The experimental validation of the model through comparison with measurements of the power distribution obtained from the IRR1 facility, as presented in Figures 14 and 15, enables the prediction of the PPF in other regions within the FA with a high degree of confidence. This experimental validation of the model is crucial as it provides a means to assess its accuracy and predict the system's behavior in regions that are not directly accessible to measurement instrumentation.

The study found that the FA's proximity to strong absorbers significantly affects the local PPF near the flux trap and the total power density within the FA. The results, presented in Figures 8 and 10, show that the local PPF near the flux trap decreases dramatically when the FA is placed close to strong absorbers. Additionally, the proximity of the FA to the graphite reflector was shown to flatten the power distribution but increase the total power in the plate, as demonstrated in Figures 11 and 12. These findings were demonstrated for both horizontal and axial orientations. These results emphasize the importance of considering the

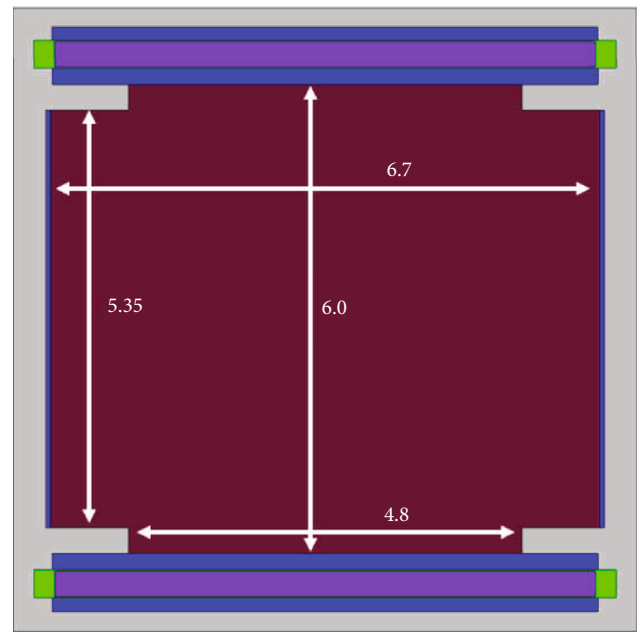

Figure 18: Geometry of a special FA with beryllium element, where the dark red, violet, and green are beryllium, the absorber, and nickel, respectively. All dimensions are given in cm.

proximity of the FA to strong absorbers and neutron reflectors in the design and operation of nuclear reactors to ensure adequate safety margins and optimize performance.

The conclusions drawn from this study have relevance to other fuel types and may provide deeper insights and understanding of the power-peaking behavior near flux traps in other reactors. This study also provides insights into the experimental measurement of this behavior, its computational simulations, and its mitigation. The results of the study indicate that the proximity of the FA to strong absorbers and reflectors can significantly impact the local PPF and power density, suggesting that such factors should be considered when designing and operating nuclear reactors of different types. Additionally, high-fidelity models, such as the Monte Carlo model used in this study, are necessary for accurately predicting the behavior of the PPF in such cases. Overall, the findings of this study may be useful for optimizing reactor design and operation and assessing the safety margins in reactors with similar characteristics.

Appendix

A. Material Composition and Geometry

The materials' isotopic compositions used in the simulation are given in Table 4. The geometric specifications of a single fuel plate (a unit cell), a control blade, and the beryllium block are shown in Figures 16–18, respectively.

Abbreviations

FA: Fuel assembly
MTR: Material test reactor
PPF: Power peaking factor
IRR1: Israel research reactor 1.

Data Availability

The experimental and numerical data used to support the findings of this study are included within the article.

Conflicts of Interest

The authors declare that they have no conflicts of interest.

Acknowledgments

This research was supported by the Pazy Research Foundation.

References

[1] R. D. Lawrence, "Progress in nodal methods for the solution of the neutron diffusion and transport equations," *Progress in Nuclear Energy*, vol. 17, no. 3, pp. 271–301, 1986.

[2] K. S. Smith, "Assembly homogenization techniques for light water reactor analysis," *Progress in Nuclear Energy*, vol. 17, no. 3, pp. 303–335, 1986.

[3] T. M. Sutton and B. N. Aviles, "Diffusion theory methods for spatial kinetics calculations," *Progress in Nuclear Energy*, vol. 30, no. 2, pp. 119–182, 1996.

[4] K. S. Smith, "Nodal diffusion methods and lattice physics data in LWR analyses: understanding numerous subtle details," *Progress in Nuclear Energy*, vol. 101, pp. 360–369, 2017.

[5] L. M. Grossman and J. P. Hennart, "Nodal diffusion methods for space-time neutron kinetics," *Progress in Nuclear Energy*, vol. 49, no. 3, pp. 181–216, 2007.

[6] K. Koebke and M. R. Wagner, "The determination of the pin power distribution in a reactor core on the basis of nodal coarse mesh calculations," *Atomkernenergie*, vol. 30, no. 2, pp. 136–142, 1977.

[7] K. R. Rempe, K. S. Smith, and A. F. Henry, "SIMULATE-3 pin power reconstruction: methodology and benchmarking," *Nuclear Science and Engineering*, vol. 103, no. 4, pp. 334–342, 1989.

[8] P. M. Bokov, D. Botes, R. H. Prinsloo, and D. I. Tomašević, "A multigroup homogeneous flux reconstruction method based on the ANOVA-HDMR decomposition," *Nuclear Science and Engineering*, vol. 197, no. 2, pp. 308–332, 2023.

[9] GIF, "A Technology Roadmap for Generation IV Nuclear Energy Systems," *GIF-002-00. Generation IV International Forum*, 2002, https://www.gen-4.org/gif/jcms/c_40481/technology-roadmap.

[10] G. Locatelli, M. Mancini, and N. Todeschini, "Generation IV nuclear reactors: current status and future prospects," *Energy Policy*, vol. 61, pp. 1503–1520, 2013.

[11] GIF, "A Technology Roadmap Update for Generation IV Nuclear Energy Systems," *GIF-002-00. Generation IV International Forum*, 2014, https://www.gen-4.org/gif/jcms/c_60729/technology-roadmap-update-2013.

[12] GIF, "GIF 2020 Annual Report. Generation IV International Forum," 2020, https://www.gen-4.org/gif/jcms/c_178290/gif-2020-annual-report.

[13] J. Leppänen, M. Pusa, T. Viitanen, V. Valtavirta, and T. Kaltiaisenaho, "The serpent Monte Carlo code: status, development and applications in 2013," *Annals of Nuclear Energy*, vol. 82, pp. 142–150, 2015.

[14] F. Brown, B. Kiedrowski, and J. Bull, *MCNP5-1.60 release notes. Report No LA-UR-10e06235*, Los Alamos National Laboratory, Los Alamos, NM, 2010.

[15] P. K. Romano, N. E. Horelik, B. R. Herman, A. G. Nelson, B. Forget, and K. Smith, "OpenMC: A state-of-the-art Monte Carlo code for research and development," *Annals of Nuclear Energy*, vol. 82, pp. 90–97, 2015.

[16] S. C. Shaner, *Development of high fidelity methods for 3D Monte Carlo transient analysis of nuclear reactors, [Ph.D. thesis]*, Massachusetts Institute of Technology. Department of Nuclear Science and Engineering, 2018, http://hdl.handle.net/1721.1/119034.

[17] L. Deng, G. Li, B. Y. Zhang et al., "A high fidelity general purpose 3-D Monte Carlo particle transport program JMCT3.0," *Nuclear Science and Techniques*, vol. 33, no. 8, p. 108, 2022.

[18] J. Yu, J. Wilson, B. Forget, A. J. Dave, K. Sun, and B. Phillips, "Experimental validation of a high fidelity Monte Carlo neutron transport model of the MIT graphite exponential pile," *Progress in Nuclear Energy*, vol. 152, article 104368, 2022.

[19] C. Castagna and E. Gilad, "Study of radionuclide inventory in nuclear fuel under uncertainties in boron concentration using high-fidelity models," *International Journal of Energy Research*, vol. 46, no. 6, pp. 8007–8019, 2022.

[20] A. S. Ivanov, *High fidelity Monte Carlo based reactor physics calculations, [Ph.D. thesis]*, Karlsruher Institut für Technologie (KIT), 2015.

[21] K. Yoshioka, M. Yamaoka, K. Hiraiwa, and T. Kitada, "Streaming effect of void reactivity in LWR critical experiments with streaming channel," *Nuclear Science and Engineering*, vol. 195, no. 1, pp. 101–117, 2021.

[22] P. Savva, S. Chatzidakis, M. Varvayanni et al., "Optimized flux trap dimensions in a research reactor core," *Nuclear Technology*, vol. 188, no. 3, pp. 322–335, 2014.

[23] K. Routsonis, S. Stoulos, A. Clouvas, N. Catsaros, M. Varvayianni, and M. Manolopoulou, "Flux trap effect study in a sub-critical neutron assembly using activation methods," *Radiation Effects and Defects in Solids*, vol. 171, no. 9-10, pp. 746–753, 2016.

[24] P. T. Petkov and S. Mittag, "VVER-1000 radial reflector modeling by diffusion nodes," *Progress in Nuclear Energy*, vol. 48, no. 8, pp. 764–772, 2006.

[25] V. Filonov, Y. Filonova, Y. Dubyk, and A. Bohdan, *Calculation of VVER-1000 core baffle temperature distribution for its swelling assessment*, vol. 2020, no. 1, 2020Odes'kyi Politechnichnyi Universytet Pratsi, 2020, https://link.gale.com/apps/doc/A629497680/AONE?u=bengurion&sid=googleScholar&xid=18410072.

[26] T. Andersson, J. Almberger, and L. Björnkvist, "A decade of assembly bow management at Ringhals," in *Proceedings of IAEA Technical Meeting on Structural Behaviour of Fuel Assemblies for Water Cooled Reactors, Cadarache, 2004*, vol. 1454, pp. 129–136, IAEA-TECDOC, 2005.

[27] A. Horváth and B. Dressel, "On numerical simulation of fuel assembly bow in pressurized water reactors," *NuclearEngineering and Design*, vol. 265, pp. 814–825, 2013.

[28] J. Li, D. Rochman, A. Vasiliev et al., "Bowing effects on isotopic concentrations for simplified PWR assemblies and full cores," *Annals of Nuclear Energy*, vol. 110, pp. 1023–1029, 2017.

[29] S. de Lambert, G. Campioni, V. Faucher, B. Leturcq, and J. Cardolaccia, "Modeling the consequences of fuel assembly bowing on PWR core neutronics using a Monte-Carlo code," *Annals of Nuclear Energy*, vol. 134, pp. 330–341, 2019.

[30] C. Wan, L. Guo, and J. Bai, "Method research and effect analysis of fuel-assembly bowing on neutron-physics simulations of HPR1000," *Annals of Nuclear Energy*, vol. 182, article 109616, 2023.

[31] M. Margulis, P. Blaise, F. Gabrielli, A. Gruel, F. Mellier, and E. Gilad, "The path for innovative severe accident neutronics studies in ZPRs. Part I.1- analysis of SNEAK-12A experiments for core disruption in LMFBRs," *Progress in Nuclear Energy*, vol. 94, pp. 106–125, 2017.

[32] M. Margulis, P. Blaise, and E. Gilad, "Modeling representative gen-IV molten fuel reactivity effects in the ZEPHYR fast/thermal coupled ZPRs. Part I-assembly level," *International Journal of Energy Research*, vol. 42, no. 5, pp. 1950–1972, 2018.

[33] T. Haga, "Effect of water gaps on various nuclear parameters of a light-water reactor," *Nuclear Science and Engineering*, vol. 38, no. 2, pp. 104–113, 1969.

[34] A. Franzén, *Evaluation of fuel assembly bow penalty peaking factors for Ringhals 3, [M.S. thesis]*, Uppsala University, 2017, UPTEC ES 17 037.

[35] D. Rochman, P. Mala, H. Ferroukhi et al., "Bowing effects on power and burn-up distributions for simplified full PWR and BWR cores," in *International Conference on Mathematics & Computational Methods Applied to Nuclear Science & Engineering*, Jeju, Korea, 2017.

[36] G. Rudstam, P. I. Johansson, O. Tengblad, P. Aagaard, and J. Eriksen, "Beta and gama spectra of short-lived fission products," *Atomic Data and Nuclear Data Tables*, vol. 45, no. 2, pp. 239–320, 1990.

[37] I. Matsson and B. Grapengiesser, "The shut-down of the Barsebäck 1 BWR: a unique opportunity to measure the power distribution in nuclear fuel rods," *Annals of Nuclear Energy*, vol. 33, no. 13, pp. 1091–1101, 2006.

[38] M. Košťál, M. Švadlenková, and J. Milčák, "Absolute determination of power density in the VVER-1000 mock-up on the LR-0 research reactor," *Applied Radiation and Isotopes*, vol. 78, pp. 38–45, 2013.

[39] P. Andersson and S. Holcombe, "A computerized method (UPPREC) for quantitative analysis of irradiated nuclear fuel assemblies with gamma emission tomography at the Halden reactor," *Annals of Nuclear Energy*, vol. 110, pp. 88–97, 2017.

[40] M. Švadlenková, L. Heraltová, V. Juříček, M. Košťál, and E. Novák, "Gamma spectrometry of short living fission products in fuel pins," *Nuclear Instruments and Methods in Physics Research Section A: Accelerators, Spectrometers, Detectors and Associated Equipment*, vol. 739, pp. 55–62, 2014.

[41] T. Makmal, O. Aviv, and E. Gilad, "A simple gamma spectrometry method for evaluating the burnup of MTR-type HEU fuel elements," *Nuclear Instruments and Methods in Physics Research Section A: Accelerators, Spectrometers, Detectors and Associated Equipment*, vol. 834, pp. 175–182, 2016.

[42] A. Krakovich, O. Aviv, L. Danon et al., "Depletion measurements using a new gamma transparency method of irradiated MTR-type fuel assemblies," *Detectors and Associated Equipment*, vol. 903, pp. 224–233, 2018.

[43] L. A. A. Terremoto, C. A. Zeituni, J. A. Perrotta, and J. E. R. da Silva, "Gamma-ray spectroscopy on irradiated MTR fuel elements," *Nuclear Instruments and Methods in Physics Research Section A: Accelerators, Spectrometers, Detectors and Associated Equipment*, vol. 450, no. 2-3, pp. 495–514, 2000.

[44] I. Neder, H. Hirshfeld, A. Krakovich, and N. Hazenshprung, *Research Reactor Benchmarking Database: Facility Specification and Experimental Data (Revision). 480 (Rev.1)*, International Atomic Energy Agency, Vienna, 2022, https://www.iaea.org/publications/14855/research-reactor-benchmarking-database-facility-specification-and-experimental-data-revision.

[45] M. V. Mora, A. G. Padilla, J. L. C. Palomino, and L. A. A. Terremoto, "Nondestructive burnup measurements by gamma-ray spectroscopy on spent fuel elements of the RP-10 research reactor," *Progress in Nuclear Energy*, vol. 53, no. 4, pp. 344–353, 2011.

[46] D. A. Brown, M. B. Chadwick, R. Capote et al., "ENDF/B-VIII.0: the 8th major release of the nuclear reaction data library with CIELO-project cross sections, new standards and thermal scattering data," *Nuclear Data Sheets*, vol. 148, pp. 1–142, 2018.

[47] S. C. van der Marck, "Benchmarking ENDF/B-VII.1, JENDL-4.0 and JEFF-3.1.1 with MCNP6," *Nuclear Data Sheets*, vol. 113, no. 12, pp. 2935–3005, 2012.

[48] M. Shibayama, M. Nagao, S. Okabe, and T. Karino, "Evaluation of incoherent neutron scattering from softmatter," *Journal of the Physical Society of Japan*, vol. 74, no. 10, pp. 2728–2736, 2005.